Improved spark and ember detection using stationary wavelet transforms

L. László Zsolt Szabó, J. János Vincze, L. László Csernoch, P. Péter Szentesi

www.elsevier.com/locate/yjtbi

Improved spark and ember detection using stationary wavelet transforms

László Zsolt Szabó, János Vincze, László Csernoch, Péter Szentesi

PII: S0022-5193(10)00188-8
DOI: doi:10.1016/j.jtbi.2010.04.005
Reference: YJTBI 5954

To appear in: *Journal of Theoretical Biology*

Received date: 9 February 2010
Revised date: 31 March 2010
Accepted date: 6 April 2010

Cite this article as: László Zsolt Szabó, János Vincze, László Csernoch and Péter Szentesi, Improved spark and ember detection using stationary wavelet transforms, *Journal of Theoretical Biology*, doi:10.1016/j.jtbi.2010.04.005

Improved spark and ember detection using stationary wavelet transforms

László Zsolt Szabó[1,2], János Vincze[1], László Csernoch[1], Péter Szentesi[1]

[1]*Department of Physiology, Medical and Health Science Centre, University of Debrecen, Debrecen, Hungary*

[2]*Department of Electrical Engineering, Sapientia Hungarian University of Transylvania, Târgu Mureş, Romania*

Phone: +36(52)255-575

Fax: +36(52)255-116

E-mail: szp@phys.dote.hu

URL: http://phys.dote.hu/

Abstract

Calcium sparks and embers are localized intracellular events of calcium release in muscle cells studied frequently by confocal microscopy using line-scan imaging. The large quantity of images and large number of events require automatic detection procedures based on signal processing methods. In the past decades these methods were based on thresholding procedures. Although recently wavelet transforms were also introduced, they have not become widespread. We have implemented a set of algorithms based on one and two dimensional versions of the à trous wavelet transform. The algorithms were used to perform spike filtering, denoising and detection procedures. Due to the dependence of the algorithms on user adjustable parameters, their effect on the efficiency of the algorithm was studied in detail. We give methods to avoid false positive detections which are the consequence of the background noise in confocal images. In order to establish the efficiency and reliability of the algorithms, various tests were performed on artificial and experimental images. Spark parameters (amplitude, full width at half maximum) calculated using the traditional and the wavelet methods were compared. We found that the latter method is capable of identifying more events with better accuracy on experimental images. Furthermore, we extended the wavelet based transform from calcium sparks to long-lasting small-amplitude events as calcium embers. The method not only solved their automatic detection but enabled the identification of events with

small amplitude that otherwise escaped the eye, rendering the determination of their characteristic parameters more accurate.

Keywords: calcium spark, ember, automatic detection, wavelet analysis

Introduction

The key step in excitation-contraction coupling of muscle cells is the increase in intracellular calcium concentration. In skeletal muscle calcium ions are released from their internal stores, the sarcoplasmic reticulum through calcium release channels (ryanodine receptors; RyR). The opening of one or a few RyR gives rise to localized calcium release events (LCRE; Cheng 1993; Schneider 1996) which are assumed to be the building blocks of the global calcium signal. To study these events confocal microscopy and calcium sensitive fluorescent dyes are used (e.g. Klein and Schneider 2006; Csernoch 2007; Cheng and Lederer 2008).

Due to the spatial and temporal characteristics of the events seen in line-scan (x-t) images they have been termed calcium sparks (high amplitude and short duration events; Cheng et al. 1993; Schneider and Klein 1996) or embers (small amplitude and long lasting events; González et al. 2000) (for recent reviews see e.g. Csernoch 2007; Cheng and Lederer, 2008). In these studies large quantities of images are produced, hundreds or thousands of events are analyzed, and statistical methods are used because of the bias introduced in the imaging and calculation processes.

Therefore, to detect calcium release events on confocal images, automatic detection methods have been developed. The goal of these algorithms is to detect and then isolate the area of each event from the noisy background, and, finally, to extract the characteristic parameters of the events. Most of these methods are based on a double threshold algorithm (this will be referred to as the *conventional method*) proposed by Cheng et al. (1999). Modified versions of the algorithm

were used in several studies (Ríos et al. 2001; Zhou et al. 2003; Sebille et al. 2005; Picht et al. 2007). However, due to the unreliable detection caused by the large variety of event morphology – especially those of embers in images from mammalian muscles – and the presence of various noise patterns, emphasis has also been placed on interactive procedures (manual selection of regions of interest and removing false positive detections).

To overcome these difficulties, methods based on wavelet transforms were also introduced in recent years for image enhancement and detection (Wegner et al. 2006; 2007). Wavelet transforms are time-frequency signal decomposition methods, their theory has been developed starting from the mid 1980's. In biomedical image processing wavelets are used for image enhancement, noise reduction and object detection (Unser and Aldroubi 1996). Although the à trous wavelet transform has excellent image enhancing and object detection characteristics on noisy images, to achieve fully automatic detection for events with variable size, parameters of the algorithm have to be properly adjusted. For images burdened with photon or shot noise tuning of the algorithm to achieve reliable detection brings up further difficulties.

Nevertheless, a fully automatic detection remains the main goal of these procedures. In case of sparks, current methods are able to detect events reliably enough to analyze data without manual intervention. However, in case of embers, previously described algorithms did not provide satisfactory results unless manual detection was also included.

We have developed a program in MATLAB (The MathWorks Inc., Natick, USA) to have a Graphical User Interface to carry out calcium event detection. The program uses wavelet based analysis, utilizing the à trous transform with cubic B-spline as scaling function. This transform has been proposed by Starck (1993) and

his coworker, Murtagh (1994) in astronomical image analysis and was first introduced by Wegner and coworkers (2006) for confocal images in calcium spark analysis. While using the conventional method manual user intervention was necessary to modify automatically selected events, with the wavelet based analysis developed here a fully automatic analysis has been achieved for sparks and an essentially automatic analysis has been achieved for embers.

We designed procedures to test the algorithm and compared the results with previous works and the conventional method. Since experimental images may contain various noise patterns, derived mostly from shot noise produced by the detector, we give a method to use the algorithm on noisy experimental images. Moreover, we test the algorithm for simultaneous detection of high and low amplitude events, and thus propose procedures to detect embers, when both sparks and embers are present on the same experimental image.

Methods

The algorithm was tested on both experimental and simulated images. The latter, with noisy backgrounds generated by the computer, were used to establish the basic values for the parameters of the algorithm. Modified experimental images were then used to study the effects of real noise patterns especially that of shot noise, on the detection process. Finally, a set of experimental images were used to evaluate the detection methods for embers.

Implementation of the traditional method

The implementation of the traditional method is a modified version of the algorithm given in a previous work (Cheng et al. 1999). In brief, the original F(x,t) image is filtered with a 3x3 median filter. Pixels above $mean + CRI \cdot \sigma$ are excluded from the image. *CRI* is an adjustable parameter between 1.6 and 2.0; the

mean and standard deviation (σ) is calculated for each spatial position (pixels at a given location at different points in time). A binary mask is formed from the excluded pixels, and continuous regions are searched for to give a binary mask of potential events. Then the image is normalized to the mean of the baseline fluorescence for each spatial position. Values $mean_2$ and σ_2 are calculated for the normalized image (excluding regions of potential LCRE). A region is accepted as an LCRE, if pixel values above $mean_2 + CRI_2 \cdot \sigma_2$ exist in the region. The criterion CRI_2 is a number above 3, for best detection CRI_2 between 3.4 and 3.7 is used. The test for pixels above CRI_2 is a simple test for existence of pixels or might be a strict test for continuous regions also.

Implementation of the à trous wavelet transform for spark detection

The algorithm used here is an implementation of the à trous wavelet transform (Holschneider et al. 1989, Mallat 1999, Shensa 1992). We followed the implementation that Starck (1993; Starck and Murtagh 1994) used for denoising and object detection in astronomical images. As a scaling function the transform uses the B-spline of degree 3 (Starck 1993) utilizing its multi-resolution properties (Unser 1997). The details of the transform are presented in Appendix 1. To handle the boundaries when performing the convolution one can use either symmetric or circular continuity, it has little influence on the wavelet coefficients (not shown). In our implementation the circular convolution was used. We demonstrate the results of the application of the two-dimensional wavelet transform on a synthetic image containing sparks of various sizes in Fig. 1.

Image denoising

For denoising the multiresolution support (Starck and Murtagh 1998a) based on the à trous transform was used. Applying the transform for L successive levels

and then rebuilding the signal with the inverse transform from levels limited by a proper threshold, gives the denoised signal. Threshold selection is thus a vital step in this method. The selection of threshold values is derived from the standard deviation of the noise in the signal (Starck and Murtagh 1998a; Starck et al. 1998b). The algorithm in detail is presented in Appendix 2, and contains a user adjustable parameter δ, to control the threshold level.

Detection algorithm for sparks

The same wavelet transform was used for the detection procedure, but now starting with the denoised image. A thresholding value T_S is applied for each wavelet plane,

$$T_{Sj} = \sigma_j \cdot \tau, \quad (1)$$

where σ_j is the standard deviation of noise for level j (for details see Appendix 2), and τ is a user adjustable parameter. This results in the construction of binary masks for each plane. Small sized (in terms of signal processing high frequency) events as sparks appear on planes 2 and 3, while larger sized (lower frequencies) events as embers, on higher level planes (see section *Automatic ember detection* in *Results*). In case of sparks, from the binary masks of level 2 and 3 (through a logical or operation) the connecting areas are formed, limiting the high frequency transition borders of sparks. For experimental images with less noise wavelet level 4 might also be used (Fig. 1).

Besides the areas containing LCRE, small areas may also be detected as events, due to specific noise patterns. These should, therefore, be discarded. When used for object detection, the à trous wavelet method is not robust enough in relation to false positive detections. High amplitude, stand-alone pixels together with noise patterns (2-3 neighboring pixels of higher value than background mean) can

disturb the detection process (Starck and Murtagh 2002). These appear frequently on fluorescence images with higher levels of shot noise.

As a measure of the detected area the number of pixels forming the connected area is thus introduced, and is termed *event size*. When performing the detection, events with sizes below a user adjustable β are discarded; hence, β is the third parameter of the algorithm.

Event parameter calculation

Sparks

For sparks, event parameters were calculated according to the usual procedure (Hollingworth et al. 2001). In case of the conventional method, the calculations were done on data extracted for sparks from the normalized image. In case of the wavelet method the normalized and denoised images were used for the calculations. In order to compare values obtained from the denoised data with values obtained from the normalized image in some tests the calculations were carried out for both. Event parameters, full width at half maximum (FWHM), full time at half maximum (FTHM) and amplitude, were calculated by averaging three neighboring lines in space and time, respectively, passing through the pixel within the spark mask having the highest value on the denoised image.

Embers

Before the analysis of the parameters of embers, background fluorescence estimates were updated for each spatial position from the mean fluorescence level of pixels not within a spark or ember mask. The raw image was then renormalized with the updated background level. This normalized image (F_{ne}), now correctly representing embers, was used to calculate the parameters as well as to recalculate the parameters of sparks.

Within the ember mask, the beginning and the end of the plateau phase were marked by the positions where the pixel values reach 80% of the maximal amplitude. We consider the duration of the ember to be the temporal distance between these two marks. All pixel values of F_{ne} between the two marks and not within a spark area were averaged in the spatial domain, showing the spatial distribution of fluorescence during the plateau phase of the ember. A Gaussian fit was applied to these mean values, from which the FWHM and amplitude parameters were derived (see e.g. Lukacs et al. 2008).

Images used for the evaluation of the algorithms

Experimental procedures for obtaining images containing sparks

Skeletal muscle fibers isolated from frogs or rats were loaded with 0.1 mM Fluo-3 to record LCRE. Images were captured using an LSM 510 META laser scanning confocal microscope (Zeiss, Oberkochen, Germany) as described earlier (Lukacs et al. 2008). In brief, line-scan images were taken at 1.54 ms/line and 512 pixels/line (pixel size 0.142 μm) with a 63x water immersion objective (1.2 n.a., Zeiss). Fluo-3 was excited with an Argon ion laser (at 488 nm), emitted light was collected through a band-pass filter and digitized at 12 bit.

The noise level of the image – expressed as the ratio of mean (m) and standard deviation (σ) of the background of the image – is an important parameter of algorithm testing. We will refer to it as signal-to-noise ratio of the background $BSNR = m/\sigma$. For experimental images, this was calculated by excluding pixels containing the events. In our experiments (including 700 randomly selected images into the analysis) BSNR varied between 3.2 and 5.4. Consequently, we will consider in our tests BSNR of 2.5 as the worst case, 3.5 as intermediate and 4.5 as good experimental conditions.

Artificial images

We used two methods to construct the background for our simulated images. First, the background was approximated by a generated noise with Gaussian distribution (e.g. Cheng et al. 1999; Wegner et al. 2006). This is a good approximation for images with low levels of shot noise. Second, we used experimental images to reconstruct the heavy shot noise patterns. Images used to generate such a background were first tested for having no positive detection of LCRE. Moreover, the scan lines were shuffled randomly to eliminate the possibility of undetected sparks in the image.

In order to test the accuracy of detecting sparks, synthetic model sparks were embedded in the background. The model spark (see e.g. Fig. 6 insets) was obtained by averaging the image of 10 experimental sparks (similar size in x and t directions) and smoothing the obtained image, and had a FWHM of ~1.7 μm, FTHM of ~9 ms and a duration of ~14 ms, values which correspond to sparks detected in our experimental images. It was then scaled to have various amplitudes. The sparks, six for each image, were distributed randomly in the image; no overlapping regions between sparks were permitted (see e.g. Fig. 1*a*).

Images containing embers

Since embers are more diverse in their morphology than sparks, we decided not to generate simulated images containing embers, but to evaluate the effectiveness of the detection method on a set of images from experiments containing embers. We have previously shown that the scorpion toxin maurocalcine causes frequent long lasting calcium release events (embers) on skeletal muscle fibers (see e.g. Lukacs et al. 2008). A set of 74 images from these experiments were used to evaluate the detection algorithm. Images contain both sparks and embers (sometimes as

combined events) with relatively high frequency and varying duration for embers made them ideal for the evaluation of the detection algorithm. Positions of the embers were manually determined by a person experienced in confocal image analysis. The result of the detection algorithm was compared to this manual selection on all images, minor differences in position were not considered as false detections since they do not affect the parameters of the ember.

Methods used to test the algorithm

To test the algorithm, 240 images with randomly embedded events (see above) were analyzed for a given set of parameters. During the repeated execution, parameters of the sparks were calculated and collected. In addition, true positive (TP; event found at the location where it was originally placed), false positive (FP; an event found at a location where originally no event was placed) and false negative (FN; an originally positioned event that was not found) detection counts were retained. To evaluate the performance and reliability of the algorithm the sensitivity (S; defined as $TP/(TP+FN)$) and the positive predictive value (PPV, as defined in signal detection theory $TP/(TP+FP)$) were calculated. To characterize the functions, the values S_{50} and PPV_{50}, defined as the relative event amplitude where S and PPV reach 50% detection probability, were used (Wegner et al. 2006). Statistical analysis was made using the SigmaStat (Aspire Software International, Ashburn, USA) program. Mann-Whitney Rank Sum test was used to compare median values and Brown-Forsythe test was used to compare standard deviations. In both cases P-value 0.001 was defined as significant.

Results

Artificial images

First the performance of the traditional and the wavelet-based detection methods were compared on artificial images (Fig. 3) where the background was generated from experimental images (panels *a* and *b*; see Methods, Simulated images) or using Gaussian noise (panels *c* and *d*). In case of the former the traditional method can be set to give satisfactory sensitivity in the 0.2-0.5 amplitude region (Fig. 3*a*), which is the region where sparks are most abundant in mammalian muscle. However, in the same amplitude region, using the same parameters (τ=3, δ=4) the positive predictive value of the detection was extremely low (less than 0.2, see Fig. 3*b*), indicating that the traditional method requires an extensive manual post-processing. In contrast, if used on simulated images with Gaussian noise, the traditional method gives high positive predictive values (Fig. 3*d*) even for low amplitude events emphasizing the importance of the noise pattern used.

While the sensitivity of the wavelet based detection method was essentially the same as that of the traditional method for both backgrounds (Fig. 3*a* and *c*), it performed substantially better in the detection of similar amplitudes on images with experimental noise. The PPV_{50} value was, in this case, lower by more than 0.3 (0.287 *vs*. 0.592) relative fluorescence units as compared to the traditional method (Fig. 3*b*). The PPV curve was, however, less steep than in case of the traditional method and it also did not match the steepness previously described in case of a similar algorithm (Wegner et al 2006). After a close examination, it was found that most of this difference could be attributed to false positive events – termed "spikes" from hereon –, which are not present on simulated images with Gaussian-distributed background noise. The background noise profile of

experimental images is not perfectly Gaussian- or even Poisson-like since high amplitude pixels are more abundant than predicted by those distributions (Fig. 2*a*). Spikes are created by the wavelet-based denoising procedure when two or three pixels with high amplitude are next to each other (Fig. 2*b-c*, *f*). These areas are then detected as false positive events (Fig. 2*d*, *h*). We compared the detection statistics of the algorithm on images with different distributions of the background noise using the same parameters (Table 1). A difference of about 0.3 units in PPV_{50} was found between images with typical experimental backgrounds (BSNR 3.24) and with Gaussian backgrounds with similar BSNR. In case of extremely noisy experimental backgrounds (BSNR < 2.5) the difference was even more pronounced (not shown).

The threshold operator

The selection of the threshold operator also has an influence on the detection of false positive events in noisy images. Of the three operators described in Appendix 2, soft thresholding produces the smoothest denoised images, but it modifies all coefficients, therefore substantially influences the calculated event parameters. The affine threshold operator produces a smoother denoised image than hard thresholding, but as an effect of inclusion of small wavelet coefficients, it is vulnerable to spikes (data not shown). Consequently, the hard threshold operator was used during the tests for image denoising.

Event size

Since spikes are generated by the denoising algorithm from a small number of neighboring pixels, they are generally smaller in time and space than detectable true events. Therefore, at first, it seemed feasible to eliminate spikes by setting a threshold – parameter β –for the size of the events during detection (Fig 2 *h*, *i*).

We evaluated different settings of β between 2 and 40 (in Fig. 4 data for β=2, 10 and 40 shown). We did not try β values lower than 2, since that would mean the inclusion of "events" containing only one pixel. Even if these hits were true positives, they would be indistinguishable from the background. With β=40 we could already reach 100% PPV at all amplitudes where we could detect events, so any further increase in β would only shift PPV_{50} to the right, but not improve sensitivity.

From the detailed evaluation of different β parameters, we concluded that size-based event selection is not an efficient method of eliminating false positive hits caused by spikes. Its moderate increase only slightly improves one part of the PPV curve (Fig. 4*b*, compare curves for $\beta = 2$ and $\beta = 10$) while a β set high enough to improve PPV substantially worsens sensitivity (Fig. 4*a*).

Spike filter

As selecting higher β values did not prove useful for the exclusion of spike-induced false positive events, we applied a filter, also based on the à trous wavelet transform to find and remove the high-amplitude pixels forming spikes. This "spike filter" was applied to the normalized image, which was obtained by the same procedure as described for the traditional method, except for the introductory median filtering and smoothing. Before denoising, the high frequency components of the image were selected (Koshino et al. 2002). The à trous transform was calculated for wavelet levels 1 and 2. For the $F_n(t,x)$ image:

$$F_n(t,x) = c_2(t,x) + \sum_{i=1}^{2} w_i(t,x) \ . \qquad (2)$$

The backward transform was performed including only the wavelet coefficients (and excluding the background obtained for level 2):

$$\mathrm{hf}(t,x) = \sum_{i=1}^{2} w_i(t,x) \ . \qquad (3)$$

Mean and standard deviation (m,σ) of $\mathrm{hf}(t,x)$ were calculated. A threshold was applied:

$$\left|hf(t,x) - m\right| > H \cdot \sigma \quad (4)$$

resulting in a binary image $B(x,y)$, revealing the high frequency pixels (edges, spikes). H is the parameter of tuning the threshold level; in case of our line-scan images the best results were obtained using values between 3.5 and 4.5.

Connected regions of 2 or more pixels were discarded. This can be achieved by convolving the binary image B with the

$$\begin{matrix} 1/9 & 1/9 & 1/9 \\ 1/9 & 1/9 & 1/9 \\ 1/9 & 1/9 & 1/9 \end{matrix} \qquad (5)$$

kernel and discarding more than 2 connected pixels. This step prevented us from smoothing regions of pixels with high fluorescence values that appear in areas of sparks. Solitaire high amplitude pixels were replaced by the mean of their 8 neighbors. The difference between results of the denoising procedure with and without spike filtering is shown in Fig. 2*f-i*.

Spike filters are generally not perfect, i.e. they may attenuate real sparks with small areas that have similar morphology to spikes, therefore, the application of the spike filter will at least slightly influence the detection of small sized events. According to our results a minor decrease in sensitivity is indeed present, but definitely not as serious as when using high β values. We obtained the best PPV for H=3.5, and even at this setting the decrease in sensitivity was moderate (data not shown).

These results could be further improved by applying the spike filter locally. Since spike-induced false positives are limited in event area, we can use the spike filter as an exclusion technique on events with small areas. In practice, the wavelet-based detection procedure is run without spike filtering, and after the detection phase one tests the small sized events for spikes (in practice we limit the test to events with areas below 50 pixel). The method is the same as described above, but the application area is limited to pixels within the detection mask of the event from the normalized image. After the test, small sized events identified as spikes are excluded, since the presence of pixels having high values in a small spark is improbable. This local test doesn't affect sparks with higher event size and amplitude.

With this improved method we could reach good spike filtering with practically no loss in sensitivity (Fig. 3*a*). In conclusion, we found that on our system the optimal parameter set for mammalian spark detection is δ=4.0, τ=3, β=2, and the spike filter should be applied with H=4.5, since it produces marked gain in PPV with no visible loss in sensitivity.

Parameters of the detected events

To test the accuracy of the calculation of event parameters, we compared the calculated parameters of differently scaled events embedded in synthetic images (Fig. 6). We used three scaled versions of the model spark: the one used in all other tests (hereafter referred to as normal sized; FWHM=1.78 μm and FTHM=18.4 ms) together with its half and double sized versions. Scaling was performed in both spatial and temporal dimensions. For each scaled version we generated images containing sparks between amplitudes 0.2 and 0.9 $\Delta F/F_0$.

We found that the calculated amplitude is a linear function of the generated amplitude at all FWHM values if the generated amplitude is at or above 0.4. Note that sparks with amplitudes higher than 0.4, could be detected with practically 100% sensitivity. The non-linearity in amplitude values below 0.4 is caused by the fact that in the case of smaller amplitudes, a spark has greater chance to be detected if positive noise is added on it. Therefore, for sparks with small amplitudes the calculated event amplitude is a biased estimate of the original event amplitude. Another interesting fact about the relationship between the generated and the calculated event amplitude is that the slope of the linear part of the function is itself a monotonically increasing function of FWHM (i.e. it was the smallest for the half sized and the largest for the double sized events). In case of the normal sized model spark, the slope was around unity (Fig. 6*b*).

We also compared the calculated FWHM values to those of the different scaled model sparks. As a general finding, the calculated FWHM at most equals that of the model spark, usually the calculation underestimates the FWHM. In case of the half sized model spark, the calculated FWHM was smaller than the original FWHM at all tested amplitudes and was independent of event amplitude (Fig. 6*a*). In the other cases the detected FWHM definitely increased as the relative amplitude of events increased, and reached 90% of the generated value at amplitude levels 0.64 and 0.4 in the case of normal (Fig. 6*b*) and double sized (Fig. 6*c*) model sparks, respectively.

Experimental images

To compare data obtained by the new wavelet-based method to data obtained by the previously used traditional method, we evaluated the results of both methods on a set of experimental images. First, the wavelet-based detection identifies a

number of events that are not found by the traditional method. In addition, both in case of the detected amplitude and in case of the detected FWHM, the mean from the wavelet-based method (0.490±0.005 $\Delta F/F_0$ and 1.90±0.01 μm) was significantly ($p<0.001$) lower than those of the traditional method (0.523±0.006 $\Delta F/F_0$ and 2.33±0.03 μm) (Fig. 5). In case of FWHM it is also apparent that the standard deviation is smaller (0.706 vs. 1.787 in the wavelet-based and in the traditional method, respectively), i.e. there are fewer events with FWHM much different from mean FWHM. This difference is also significant ($p<0.001$).

We attribute these differences mainly to two factors. First, the wavelet-based method has better sensitivity and PPV at smaller amplitudes, therefore small sparks had higher probability to be detected by the wavelet transformation. Second, the denoising produces based on the wavelet transforms generate much cleaner images than the median filter used in the traditional method therefore curve fittings are more accurate. We visually compared several sparks where the result of fitting was different for the two algorithms and verified that the fitting on the wavelet-denoised image was better.

Izu and his coworkers (1998) pointed out that if simple assumptions for the RyR hold true – the duration of all release channel openings are equal – the reciprocal of the relative number of events should be a linear function of event amplitude. As presented in Fig. 5*a* inset the relationship is a convex rather than a linear function, suggesting that the sparks were generated by channels whose open times were exponentially distributed as discussed by Izu et al. (1998).

Automatic ember detection

Image preprocessing for ember detection

Our ember detection method uses the raw fluorescence image as its input (Fig. 7*a*), but sparks are excised from it. This excision is achieved by the multiplication of the original image with the inverse of the spark mask generated in the final step of spark detection, containing 0 if a pixel is within a spark rectangle and 1 otherwise (Fig. 7*a*, rectangles). In order not to generate sharp amplitude steps causing undesired signals on lower frequency (i.e. higher) wavelet levels, pixels with zero values are filled with the values of a randomly positioned set of pixels from the same time line not within any spark rectangle. Let the image generated this way be denoted as F_e (Fig. 7*c*). Note that the described filling method also ensures that even if consecutive sparks are present in a column, they are filled with different background pixels. Without random sampling from the column, unwanted low frequency patterns may arise, significantly lowering the positive predictive value of the algorithm. This image is further enhanced by spike filtering (see section *Spike filter*), eliminating shot noise patterns that can cause a significant signal even on high wavelet levels. In conclusion, F_e is suitable for use in all further steps of ember detection.

Wavelet transform and ember detection

We propose two slightly different methods for ember detection, both based on the á trous wavelet transform. Both algorithms have clear advantages over the other, so we provide a detailed analysis and comparison of the two.

Method A – 2D wavelet transform

Due to the characteristics of the wavelet transformation, lower frequency signal components, like those representing embers, are found on higher wavelet levels.

We found in our preliminary studies that embers of typical duration (90 ms to 1300 ms, i.e. 60 to 850 pixels under the condition used here) appear mostly on the fifth wavelet level (w_5 , Fig. 7*d*) if the above-described two dimensional wavelet transform is performed. To localize embers on this wavelet plane a double thresholding is applied:

$$M_A(x,y) = \begin{cases} 0, \textit{if } w_5(x,y) < \mu \cdot \varepsilon, \\ 1, \textit{if } \mu \cdot \varepsilon \le w_5(x,y) < \mu \cdot \zeta \\ 2, \textit{if } \mu \cdot \zeta \le w_5(x,y). \end{cases}, \qquad (6)$$

where μ is the image mean, ε is the lower criterion and ζ is the higher criterion. Connected areas of $M_A \geq 1$ containing at least ten pixels with $M_A = 1$ are considered to be embers (Fig. 7*e*). For further analysis, their bounding rectangle is determined by adding 30 pixels in each temporal direction and 10 pixels in each spatial direction to the minimum bounding rectangle of the area (Fig. 7*i*; rectangles with short dashed lines).

Method B – 1D wavelet transform

In contrast to the two-dimensional wavelet transform used for spark detection and in *Method A*, in *Method B* we apply a one-dimensional wavelet transform in the time dimension on each image line separately. This choice was made to account for the spatiotemporal characteristics of embers (i.e. their width in the space domain is on the order of 25 pixels whilst their length in the time domain can be more than ten times larger) and for the lack of uniform background level in the absence of normalization.

Apart from the difference in the number of dimensions, we use the same wavelet transform and base function as described in section *Implementation of the à trous wavelet transform for spark detection*. Let the wavelet levels of the so decomposed signal be denoted as w'_k, where k is the number of the level. As

shown on Fig. 7*f-g*, embers of typical duration yield the most distinctive signal on levels 8 and 9. In case of longer embers, the signal on level 8 is more pronounced around the beginning and the end of the event and the signal on level 9 is more pronounced in the middle. We, therefore, perform double thresholding on the combined image generated by the following function from wavelet levels 8 and 9:

$$w'_{8+9} = \max(w'_8, w'_9) \ . \qquad (7)$$

The resulting mask of double thresholding (M_B) is generated using the image mean (μ), lower (ε) and higher (γ) criteria:

$$M_B(x,y) = \begin{cases} 0, \textit{if } w'_{8+9}(x,y) < \mu \cdot \varepsilon, \\ 1, \textit{if } \mu \cdot \varepsilon \le w'_{8+9}(x,y) < \mu \cdot \gamma \\ 2, \textit{if } \mu \cdot \gamma \le w'_{8+9}(x,y). \end{cases} \ . \qquad (8)$$

Again, connected areas of $M_B \geq 1$ containing at least 10 pixels with $M_B = 1$ are considered to be embers (Fig. 7*h*). For further analysis, their bounding rectangle is determined by adding 30 pixels in each temporal direction and 10 pixels in each spatial direction to the minimum bounding rectangle of the area (Fig. 7*i*; rectangles with long dashed lines).

Ember detection statistics

Detailed analysis of the events detected as embers by our algorithms shows that both algorithms are generally capable for automatic ember detection. When tested on all 74 images method B based on the 1D wavelet transform always had higher positive predictive value for a given sensitivity than method A (Fig. 8). However, method A has characteristics that can yield better detection parameters in certain applications. First, it is able to find relatively shorter, but wider events (Fig. 7*i*). Second, it is capable of detecting events that span the entire image. In conclusion, we found that images similar to those analyzed here can be most effectively

processed with method B, using parameters ε=0.015 and γ=0.035 (resulting in a PPV of 0.84 at 0.71 sensitivity). Under the same conditions method A reached 0.64 PPV at 0.73 sensitivity (ε=0.015, ζ=0.055).

We next compared the parameters of long lasting events identified by the wavelet transform to those identified by eye. First, it is important to stress that the wavelet-based method recognized more events (179 vs. 112 in the 140 images tested). It is clear from the distributions of event amplitudes presented in Fig. 9*a* that these extra events had smaller amplitudes. Noteworthy is the fact that the amplitude distribution, which had a shallow rising phase for the events identified by eye , became more exponential, as expected theoretically. This resulted in a clear change in the average amplitude to smaller values, from 0.231±0.013 to 0.197±0.009, for events identified by eye and by the wavelet method, respectively.

On the other hand, the distributions of FWHM for the two methods (Fig. 9*b*) were not as different as for the amplitudes, indicating that the extra events found by the wavelet method indeed belong to the same group as the others. This observation was confirmed by the fact that only a small, albeit significant difference was detected in the average values of FWHM, 1.93±0.05 vs. 2.09±0.04 μm.

Taken together, these observations not only confirm that the wavelet-based method is capable of identifying long lasting events as embers, but prove that it gives a more accurate detection than a simple identification by eye does.

Discussion

In this work the à trous wavelet transform was implemented to detect localized calcium release events in fluorescence images from skeletal muscle fibers. We used the transform to develop algorithms for denoising, event detection and spike

filtering. The method proved to be a valuable tool in analyzing these two-dimensional fluorescence signals (*x-t* images) embedded in a noisy background. Besides the use of the transform to detect calcium sparks – events with large amplitude and relatively short duration –, we established a procedure to isolate long lasting, low amplitude events, as embers. The results presented here imply that these multi-resolution methods are, on the one hand, adequate for analyzing confocal images and, on the other hand, indicate that they are a better choice than the traditionally applied thresholding algorithms.

Wavelet based methods in biological data/image processing have been used extensively. Nevertheless, these algorithms in calcium imaging have not gained ground, and only a few reports are available for comparison (Wegner et al. 2006; 2007). The important difference between the tests presented in those reports and the tests presented here is that we used backgrounds generated from experimental images rather than backgrounds generated using mathematical distributions. This difference becomes significant if positive predictive values and sensitivities are compared since experimental images are burdened with shot noise. Clearly, the values of PPV_{50} and S_{50} reported by Wegner and coworkers (2006) are smaller than the values obtained here with the simple (without spike filter) wavelet method. We believe that this difference is due to the presence of pixels with high fluorescence intensity in experimental images.

Importantly, therefore, if one uses the transform on experimental images from mammalian muscle images that are usually affected by high levels of shot noise , one must face the high sensitivity of the detection procedure, resulting in a large number of false positive detections (see Figs. 1-3). This renders the simple wavelet method inconvenient for event detection since an extensive manual post-processing (removing of false positive events by an experienced person) would be

required. This could explain why wavelet-based detection has not become widespread. As a result, we present here a procedure – the spike filter; also based on the wavelet method –, to avoid false positive detections. If the traditional technique for spark detection and the method based on the wavelet transform (including the spike filter) are compared, a higher sensitivity and better positive predictive values can be achieved by the latter (see Fig. 3).

We thus used data from the denoised images for calculating the parameters of calcium sparks. This permitted better curve fitting and more accurate determination of the parameters. It should be emphasized here that the amplitude was only slightly affected by the denoising, while the signal-to-noise ratios in the analyzed images had been improved. Comparing the event parameters obtained with the wavelet method to data derived with the traditional method revealed significant differences. Most importantly, a number of events that were not recognized by the traditional method - mostly events with small amplitudes (see Fig. 5a) - were clearly identified by the wavelet-based algorithms. In addition, the distribution of event parameters was more consistent for the latter, showing that the identified events are indeed derived from a single population. It is important to stress here that the distribution of FWHM obtained with the traditional method shows a slight increase at small FHWM values. This is clearly due to the fact that no manual selection of the events was permitted resulting in a number of false positive detections using the traditional method. In conclusion, the wavelet-based method provides better parameter estimation in the case of experimental images than the traditional method, because the cleaner denoised images result in better curve fitting. However, there is a significant difference in the distributions of event parameters; therefore images processed using the traditional method should

be reprocessed before comparing their results to new data obtained with the wavelet-based detection algorithm.

Previously published LCRE detection methods for *x-t* images rely on column-by-column normalization of the raw image in order to eliminate the variation of background fluorescence and produce relative fluorescence signal. This normalization technique is suitable when the combined event duration is only a fraction of the total scan time. It will; however, not produce the desired result if this condition is not fulfilled, e.g. on images containing long embers. Embers are effectively smoothed into the background and, more importantly, darker areas may appear before and after the event, rendering them undetectable by the normalization (Fig. 7*b*). Therefore, using previously published methods for spark detection, embers usually have to be manually selected on raw images. Manual selection is not only impractical on large amount of data, but may also lead to bias in ember parameters, similarly to the bias in case of spark amplitudes as described in previous studies (Song et al. 1997).

The two, wavelet-based ember detection algorithms described here proved to be effective aids in analyzing images containing embers. Although their detection efficiency (sensitivity and positive predictive value) may not be as good as those of the spark detection algorithm (compare Figs. 3 and 7), it is evident that they can greatly reduce the human workload. Under favorable circumstances, they may even be capable of reliable and fully automatic ember detection. In addition, it is clear that the parameters derived from the events identified by the wavelet method represent a more accurate estimation of the actual values than those obtained with the traditional methods.

If detection accuracy is analyzed in detail two problems with the wavelet-based detection can be identified. It is clear from the distributions presented in Fig. 9

that there are events which were identified by eye and not by the wavelet method. Individually looking at these undetected events revealed that they either represent short embers trailing a spark or were events very closely following one another. In case of the former the ember was included into the spark by the automatic detection, while in case of the latter they were taken as a single event. The number of these events was, however, small, less than 10%, rendering the detection accuracy still quite acceptable.

Despite these slight problems the methods presented here are an important step forward in automatic ember detection. Furthermore, these algorithms, especially the 1D wavelet transform based variant, can also be used as a basis for algorithms of spark detection on recently introduced high-speed line-scan images, since on those images the morphology of a spark is very similar to that of an ember if measured with a normal-speed confocal scanner.

Acknowledgements

The authors are grateful for the help of Dr. Beatrix Dienes. The work was supported by grants from the Hungarian Scientific Research Fund OTKA (K75604, NK78398) and ETT (186-09).

Appendix 1

The à trous transform is an undecimated discrete wavelet transform, consequently permits the exact temporal and spatial localization of various frequencies and signal intensities found in the analyzed data. Detailed mathematical description is given by Mallat (1999), Shensa (1992) and Bijaoui et al. (1994). We used both of the one and two dimensional à trous transform.

According to Starck and Murtagh (1994), for the one dimensional transform, the wavelet function $\psi(x)$ is defined as:

$$\frac{1}{2}\psi(\frac{x}{2}) = \phi(x) - \frac{1}{2}\phi(\frac{x}{2}) \ . \qquad \text{(a1)}$$

where $\phi(x)$ is the scaling function, satisfying the dilation equation:

$$\frac{1}{2}\phi\left(\frac{x}{2}\right) = \sum_l h(l)\phi(x-l) \ . \qquad \text{(a2)}$$

with *h* as a discrete low pass filter associated with the scaling function.

For the one dimensional case the sampled data $\{c_0(k)\}, k = 1..N$, is considered as the scalar product at pixels *k* of the function *f(x)* with the scaling function $\phi(x)$, used as a low pass filter:

$$c_0(k) = < f(x),\ \phi(x - k) > \ . \qquad \text{(a3)}$$

The low pass filtered data at a resolution level *i* and position *k* is obtained by:

$$c_i(k) = \frac{1}{2^i} < f(x), \phi(\frac{x-k}{2^i}) > \ . \qquad \text{(a4)}$$

Computationally this is obtained by the convolution:

$$c_i(k) = \sum_l h(l) c_{i-1}(k + 2^{i-1} l) \ . \qquad \text{(a5)}$$

The wavelet coefficients are resulting from the signal difference between two successive convolution steps:

$$w_i(k) = c_{i-1}(k) - c_i(k), \text{ or} \qquad \text{(a6)}$$

$$w_i(k) = \frac{1}{2^i} < f(x), \psi(\frac{x-k}{2^i}) > \ , \qquad \text{(a7)}$$

The wavelet function is defined by (a1). The calculations are reduced to the following algorithm (Starck and Murtagh 1994):

1. *i* is set to 0, and the algorithm starts with the original data set *{c_i(k)}*.

2. *i=i+1*, and a discrete convolution is carried out using the filter *h* .

3. the discrete wavelet transform is obtained after the convolution step from the difference: $w_i(k)=c_{i-1}(k)-c_i(k)$

4. If i < L, L being the level of resolution to compute, go to step 2.

5 The set $w_1, w_2, ..., w_L, c_L$ is the wavelet transform of the data. c_L is the low frequency background of the data. The algorithm is extensible to two dimensions.

As convolution masks we used the values derived from cubic B-spline: $\frac{1}{16}\times[1,4,6,4,1]$ for the one dimensional, and

$$\frac{1}{256}\times\begin{bmatrix}1 & 4 & 6 & 4 & 1\\ 4 & 16 & 24 & 16 & 4\\ 6 & 24 & 36 & 24 & 6\\ 4 & 16 & 24 & 16 & 4\\ 1 & 4 & 6 & 4 & 1\end{bmatrix} \quad \text{(a8)}$$

for the two dimensional case.

The inverse à trous transform is defined by:

$$c_0(k) = c_L(k) + \sum_{i=1}^{L} w_i(k) \ . \quad \text{(a9)}$$

The set defined by $w_i(k)$ is called wavelet plane *i*. A wavelet plane contains the same number of pixels as the original data set .

Appendix 2

In the first phase of the denoising procedure we approximate the general noise level of the image (Starck and Murtagh 1998a). This approximation is performed iteratively in the following steps:

1. Estimate the standard deviation of the noise in the original image: eliminate pixels above image $mean + 3 \cdot \sigma$ and calculate the standard deviation of the remaining pixels; we have σ_{I0}.

2. Compute the wavelet transform of the image for L levels and obtain:

$$f(x,y) = c_L(x,y) + \sum_{i=1}^{L} w_i(x,y) \quad . \qquad \text{(a10)}$$

The noise in the low frequency background c_L is negligible.

3. Set *n* to 0.

4. Compute multiresolution support *M(j,x,t)* , *j=1,L* resulted from wavelet coefficients and σ_{I_n}. Wavelet coefficients > $3 \cdot \sigma_j$ are considered significant, σ_j is calculated according to (a11).

5. A binary mask is formed. Pixels are set to 1 where *M(j,x,t)* is below threshold in each wavelet plane (insignificant wavelet coefficients that are considered belonging to noise). From pixels selected by this mask the background $c_L(x,y)$ is subtracted (the background is not included in the noise estimation.

6. *n=n+1,* compute σ_{I_n} from the selected pixels.

7. If $\left|\sigma_{I_n} - \sigma_{I_{n-1}}\right| / \sigma_{I_n} > \varepsilon$, go to step 4.

The method converges in a few steps, resulting in σ_I of the noise in the image.

After that the standard deviation of the noise σ_j for level *j* is determined from the standard deviation of the noise in the original image:

$$\sigma_j = \sigma_I \cdot \sigma_{j0} \quad , \text{(a11)}$$

where $\sigma_{j0}, j = 1, L$, is the standard deviation of wavelet transform level *j* of a Gaussian noise with standard deviation 1, and σ_I is the estimate of the standard

deviation of the noise in the original image. From this a threshold level for each wavelet level is determined:

$$T_{Dj} = \delta \cdot \sigma_j \ , \quad \text{(a12)}$$

where δ is one of the user adjustable parameters of the algorithm. The last step of the denoising algorithm is to perform thresholding on each wavelet level using one of the following functions (Jin et all. 2005).

Hard threshold:

$$g_{hT}(x) = \begin{cases} x, if \left|x\right| > T_{Dj} \\ 0, if \left|x\right| \le T_{Dj} \end{cases} . \quad \text{(a13)}$$

Soft threshold:

$$g_{sT}(x) = \begin{cases} x - T_{Dj}, if \ x \ge T_{Dj} \\ x + T_{Dj}, if \ x \le -T_{Dj} \\ 0 \ if \ \left|x\right| < T_{Dj} \end{cases} . \quad \text{(a14)}$$

Affine (firm) threshold:

$$g_{aT}(x) = \begin{cases} x, if \left|x\right| \ge T_{Dj} \\ 2 \cdot x + T_{Dj}, if \ -T_{Dj} \le x \le -{T_{Dj}}/{2} \\ 2 \cdot x - T_{Dj}, if \ {T_{Dj}}/{2} \le x \le T_{Dj} \\ 0 \ if \left|x\right| < {T_{Dj}}/{2} \end{cases} \quad \text{(a15)}$$

References

Bijaoui A, Starck JL, Murtagh F (1994) Restauration des images multi-échelles par l'algorithme à trous. Traitement du Signal 11:229-243.

Cheng H, Lederer WJ, Cannell MB (1993) Calcium sparks: elementary events underlying excitation-contraction coupling in heart muscle. Science 262:740-744.

Cheng H, Song LS, Shirokova N, Gonzalez A, Lakatta EG, Rios E, Stern MD (1999) Amplitude Distribution of Calcium Sparks in Confocal Images: Theory and Studies with an Automatic Detection Method. Biophys J 76:606-617.

Cheng H, Lederer WJ (2008) Calcium Sparks. Physiol Rev. 88:1491-1545.

Csernoch, L (2007) Sparks and embers of skeletal muscle: the exciting events of contractile activation. Pflügers Archiv: Eur J Physiol 454:869-78.

González A, Kirsch W G, Shirokova N, Pizarro G, Stern M D, Ríos E (2000) The spark and its ember. J Gen Physiol 115:139–157.

Hollingworth S, Peet J, Chandler WK, Baylor SM (2001) Calcium Sparks in Intact Skeletal Muscle Fibers of the Frog. J Gen Physiol 118:653-678.

Holschneider M, Morlet M, Kronland-Martinet R, Tchamitchian P (1989) Wavelets Time Frequency Methods and Phase Space. Springer Verlag Berlin, pp 289-297

Izu LT, Wier WG, Balke CW (1998) Theoretical Analysis of the Ca^{2+} Spark Amplitude Distribution. Biophy J 75: 1144–1162.

Jin Y, Angelini E, Laine A (2005) Wavelets in Medical Image Processing: Denoising, Segmentation, and Registration. In: Handbook of Biomedical Image Analysis, Springer, Berlin, pp 319-324

Klein MG, Schneider MF (2006) Ca^{2+} sparks in skeletal muscle (review). Progress, Biophys Mol Biol, 92:308-332.

Koshino K, Saito N, Suzuki S, Tamaki J (2002) Spike noise removal in the scanning laser microscopic image of diamond abrasive grain using a wavelet transform. Opt Commun 211:73–83.

Lukacs B, Sztretye M, Almassy J, Sarkozi S, Dienes B, Mabrouk K, Simut C, Szabo L, Szentesi P, De Waard M, Ronjat M, Jona I, Csernoch L (2008) Charged surface area of maurocalcine determines its interaction with the skeletal ryanodine receptor. Biophy J 95:3497-3509.

Mallat S G (1999) A Wavelet Tour of Signal Processing, Edition 2, Academic Press, London

Picht E, Zima A, Blatter LA, Bers DM (2007) SparkMaster - Automated Calcium Spark Analysis with ImageJ, Am J of Physiol, Cell Physiol 293:C1073-81.

Ríos E, Shirokova N, Kirsch G, Pizarro G, Stern MD, Cheng H, González A (2001) A preferred amplitude of calcium sparks in skeletal muscle. Biophys J 80:169–183.

Schneider MF, Klein MG (1996) Sarcomeric calcium sparks activated by fiber depolarization and by cytosolic Ca^{2+} in skeletal muscle. Cell Calcium 20:123-128.

Sebille S, Cantereau A, Vandebrouck C, Balghi H, Constantin B (2005) Calcium sparks in muscle cells: interactive procedures for automatic detection and measurements on line-scan confocal images series. Computer Methods and Programs in Biomedicine 77:57-70.

Shensa MJ (1992) The Discrete Wavelet Transform: Wedding the À Trous and Mallat Algorithms. IEEE T On Signal P, Vol. 40. No. 10:2464-2482.

Song LS, Stern MD, Lakatta EG, Cheng H (1997) Partial depletion of sarcoplasmic reticulum calcium does not prevent calcium sparks in rat ventricular myocytes. J Physiol 505:665-675.

Starck JL (1993) The à trous algorithm. In: ESO-MIDAS User's Guide, Volume B. ESO European Organization for Astronomical Research in the Southern Hemisphere. http://www.eso.org/sci/data-processing/software/esomidas. Accessed 26 May 2009.

Starck JL, Murtagh F (1994) Image restoration with noise suppression using the wavelet transform. Astron Astrophys 288:342-348.

Starck JL, Murtagh F (1998a) Automatic Noise Estimation from the Multiresolution Support. Publ Astron Soc Pac 110:193–199.

Starck JL, Murtagh F, Bijaoui A (1998b) Image Processing and Data Analysis: The Multiscale Approach. Cambridge University Press. London

Starck JL, Murtagh F (2002) Astronomical Image and Data Analysis, Springer, Berlin

Unser M, Aldroubi A (1996) A Review of Wavelets in Biomedical applications. P IEEE, Vol. 84, No. 4:626-638.

Unser M (1997) Ten Good Reasons for Using Spline. Proc. SPIE Vol. 3169, Wavelets Applications in Signal and Image Processing V:422-431.

Wegner FV, Both M, Fink RHA (2006) Automated Detection of Elementary Calcium Release Events Using the À Trous Wavelet Transform. Biophys J 90:2151–2163.

Wegner FV, Both M, Fink RHA, Friedrich O (2007) Fast XYT Imaging of Elementary Calcium Release Events in Muscle With Multifocal Multiphoton Microscopy and Wavelet Denoising and Detection. IEEE Transact. Med. Im. Vol. 26, NO. 7:925-934.

Zhou J, Brum G, González A, Launikonis B S, Stern M D, Ríos E (2003) Sparks and Embers of Mammalian Muscle. Properties of the Sources. J Gen Physiol 122:95–114.

Figure legends

Fig. 1 A simulated image and its wavelet decomposition. ***a*** Simulated image with Gaussian noise pattern containing 6 sparks (arrows; with relative amplitudes of 0.33, 0.45, 0.57, 0.93, 1.0 and 1.2 F_0) and one single pixel set to shot noise level. ***b-f*** Wavelet decomposition levels 1 through 5 of the simulated image. On all panels, warmer colors indicate higher values. Scale bars on panel ***b*** apply for all images.

Fig. 2 Spikes and the background noise distribution of a confocal line-scan image. ***a*** Histogram of a shot noise affected experimental image that does not contain sparks. Inset shows the histogram on an expanded *y*-scale to demonstrate the presence of pixels with high fluorescence. ***b-e*** Appearance of spikes following wavelet decomposition. ***b*** Shot noise pattern (a few neighboring pixels with high fluorescence intensity) from an experimental image. Brighter green indicates higher fluorescence intensity. ***c*** The shot noise pattern on the normalized image. ***d*** The shot noise pattern on the wavelet-denoised image. ***e*** Detection mask of the shot noise pattern obtained with the wavelet method. Scale bars in panel ***e*** apply for all images in ***b-e***. ***f*** Denoised image of the simulated image of Fig. 1*d* without the spike filter. ***g*** Denoised image of the simulated image of Fig. 1*d* with the spike filter. ***h,i*** Detection masks obtained without and with spike filter for images in ***f*** and ***g***, respectively. Arrow points to the spike caused by the shot noise. Note the lack of spike on panel ***i***. Scale bars in panel ***i*** apply for all images in ***f-i***. Color scale in panel ***f*** applies for panel ***c***, ***d***, ***f*** and ***g***.

Fig. 3 Sensitivity (***a, c***) and positive predictive values (***b, d***) as a function of event amplitude for different detection algorithms. Simulated images with synthetic model sparks on backgrounds generated from experimental images (***a, b***) and with Gaussian noise (***c, d***) were used to test the accuracy of the algorithms. Three different algorithms were tested, the traditional method (with CRI_2=3.6), the wavelet based method without and with spike filter (with H=4.5, τ=3, δ=4, wavelet levels 2 and 3). Curves for each data set were drawn by eye with S_{50} and PPV_{50} values of 0.315, 0.315, 0.325 on panel ***a***, 0.285, 0.21, 0.595 on panel ***b***, 0.3, 0.3, 0.41 on panel ***c*** and 0.23, 0.23, 0.26 on panel ***d*** for the wavelet without and with spike filter and for the traditional methods, respectively.

Fig. 4 Sensitivity (***a***) and positive predictive values (***b***) as a function of event amplitude if the events below a predefined area (event size, parameter β) are excluded. The wavelet method without the spike filter was used for event detection. Images were generated as described for Fig. 3. Results are shown for three (2, 10 and 40) different β values. Curves for each data set were drawn by eye with S_{50} and PPV_{50} values of 0.37, 0.41, 0.585 and 0.583, 0.576, 0.325 for β = 2, 10 and 40, respectively. (For further details, see text).

Fig. 5 Distribution of spark parameters, amplitude (***a***) and FWHM (***b***). Events were identified with the traditional (grey) and the wavelet based (black) methods using the spike filter for the latter. 300 images were included into the analysis. Event parameters were calculated as described in Methods. All identified events, regardless of their parameters were included into the histograms. Inset in

panel ***a*** shows the reciprocal of the relative number of events as a function of event amplitude for data in this panel.

Fig. 6 Evaluation of how the detected event parameters – amplitude (●) and FWHM (Δ) – depend on the original event parameters. Generated model sparks, shown in the insets, were scaled to have different amplitudes and then embedded in images with backgrounds generated from experimental images. Horizontal short dashed lines in ***a-c*** give the FWHM of the original sparks. Long dashed lines are linear fits to data points obtained for sparks with amplitudes 0.4 and above with slopes of 0.48, 0.76 and 1.02, respectively. Scale bars on panel ***b*** and the color scale in panel ***c*** apply for all images.

Fig. 7 Detection of embers using the wavelet method. ***a*** Sparks and embers on an experimental image. As a first step sparks are identified (rectangles). ***b*** Normalized image, note the problem of normalization at the spatial position of the ember. ***c*** Image with excised sparks. ***d*** Wavelet transform – level 5 – of the image in panel ***c***. ***e*** Mask obtained from the image in panel ***d*** with the double threshold method. ***f-g*** Wavelet transform levels 8 and 9 of the image in panel ***c***. ***h*** Mask obtained with a simple threshold method from the images in panels ***f*** and ***g***. ***i*** Identified sparks and embers, the latter are marked by dashed rectangles. For further details, see text. Scale bars and the color scale on panel ***c*** apply for panels ***a-c***, ***i***.

Fig. 8 Accuracy of ember detection using one- and two-dimensional wavelet transforms. For testing 74 experimental images were used. Note that the 1D wavelet transform (method B) always had a higher positive predictive value for a given sensitivity than did the 2D based transform (method A). For details on methods A and B, see text.

Fig. 9 Distribution of ember parameters, amplitude and FWHM. Events were identified with the traditional and the wavelet based methods using the spike filter for the latter. 140 images were included into the analysis. Event parameters were calculated as described in Methods. All identified events, regardless of their parameters were included into the histograms.

Table 1. Effect of background noise on detection* statistics.

Background noise distribution	**BSNR**	**S_{50}**	**PPV_{50}**
Gaussian	2.0	0.37	0.28
Experimental	2.38	0.47	0.90
Gaussian	2.5	0.37	0.28
Experimental	3.24	0.35	0.58
Gaussian	3.5	0.30	0.23

*Parameters used in the wavelet-based detection were $\delta = 3.5$; $\tau = 3.5$.

Figure 1

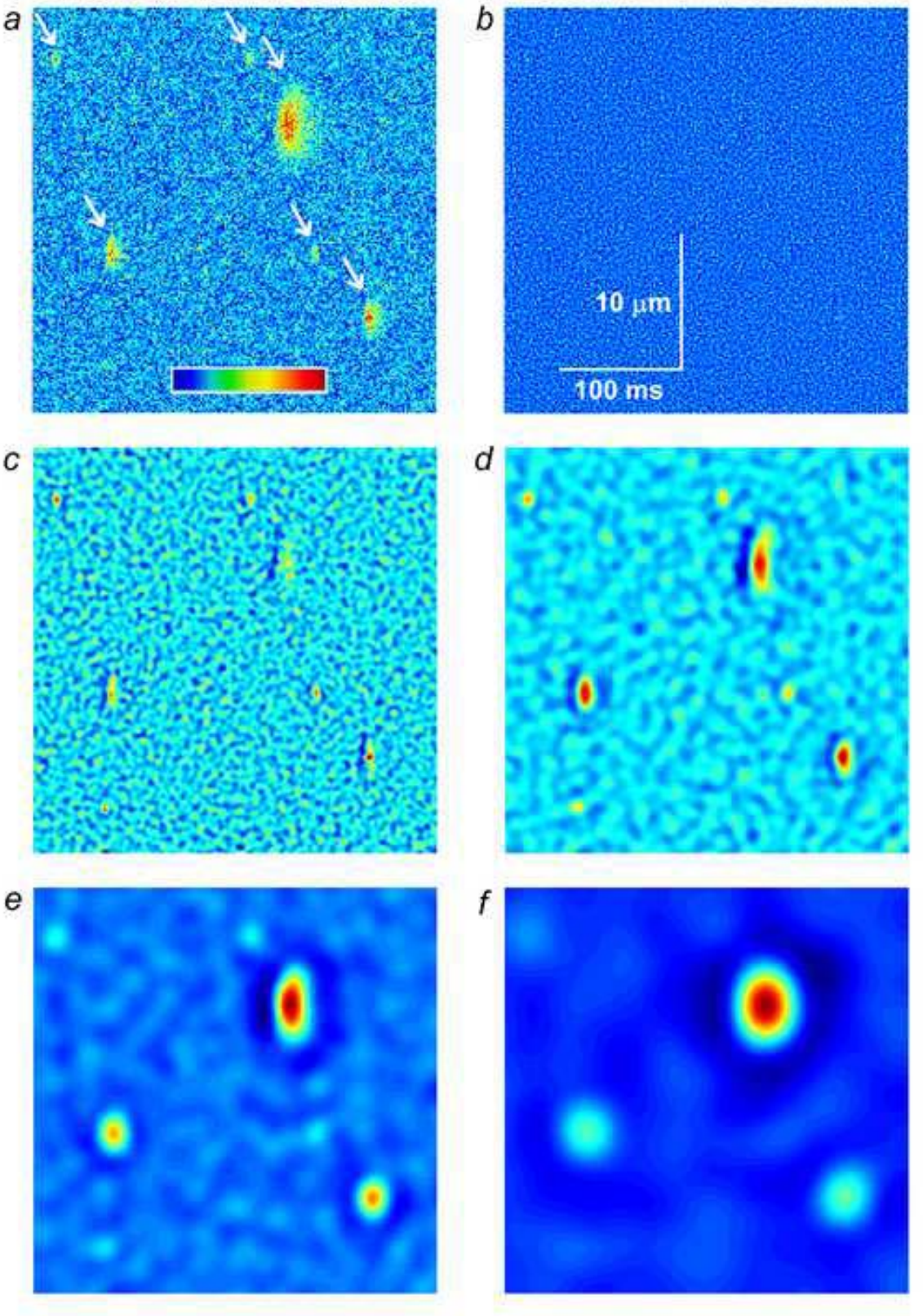

Figure 2

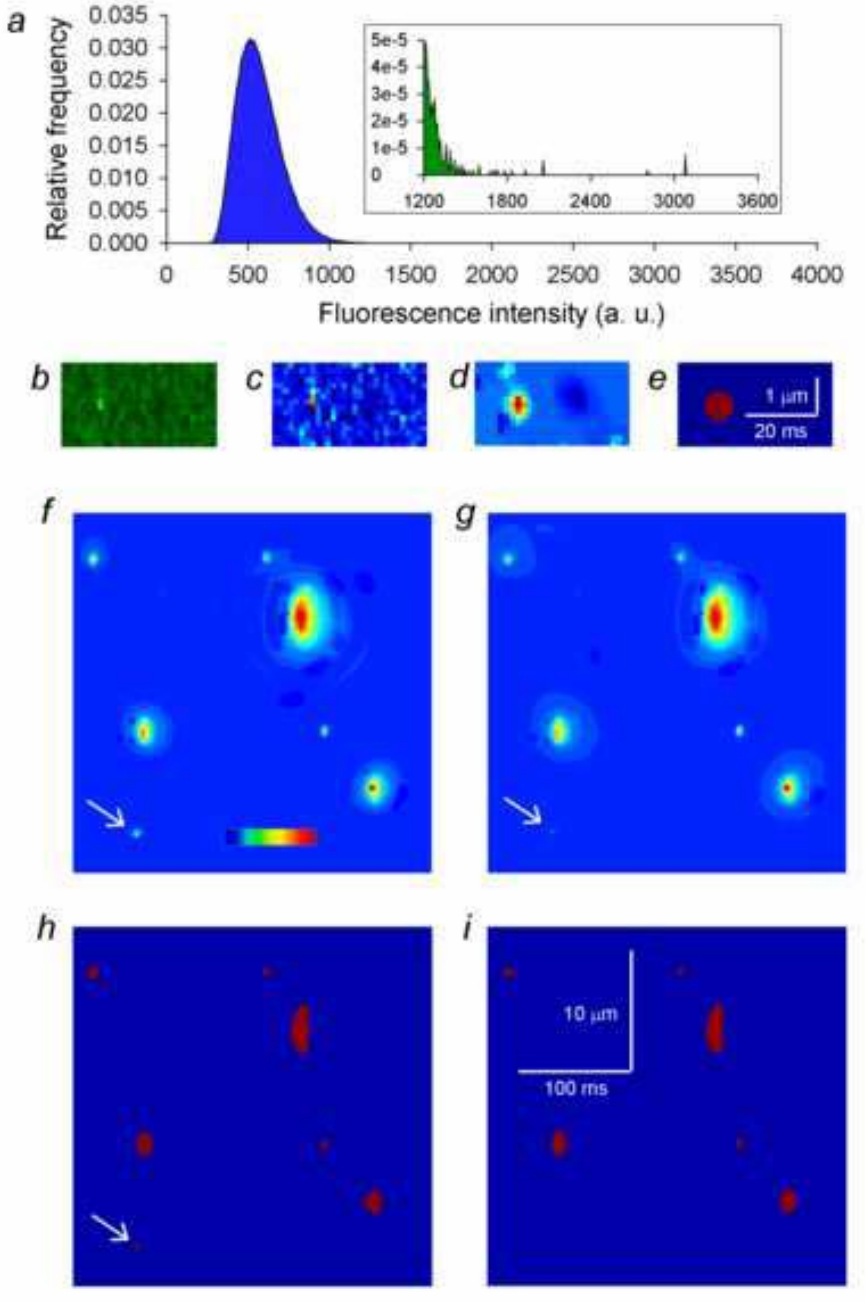

Figure 3

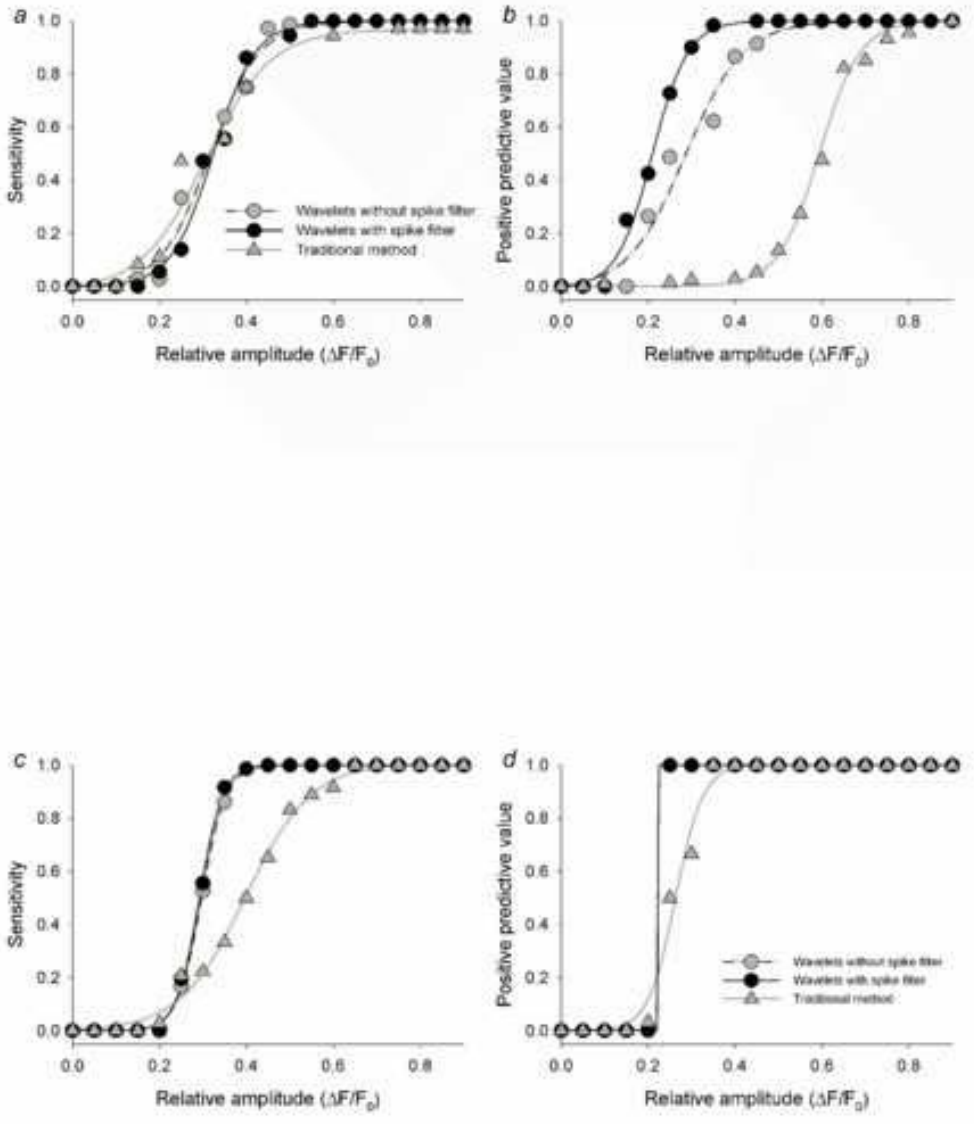

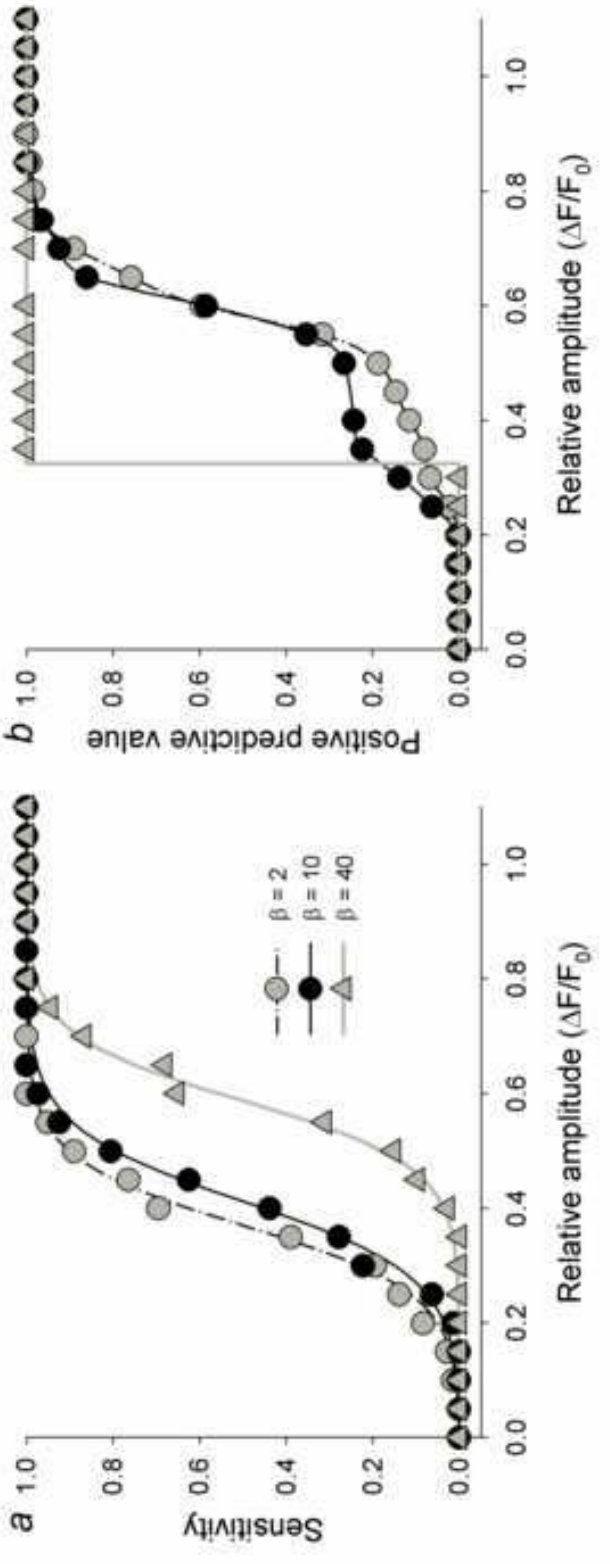

Figure 4

Figure 5

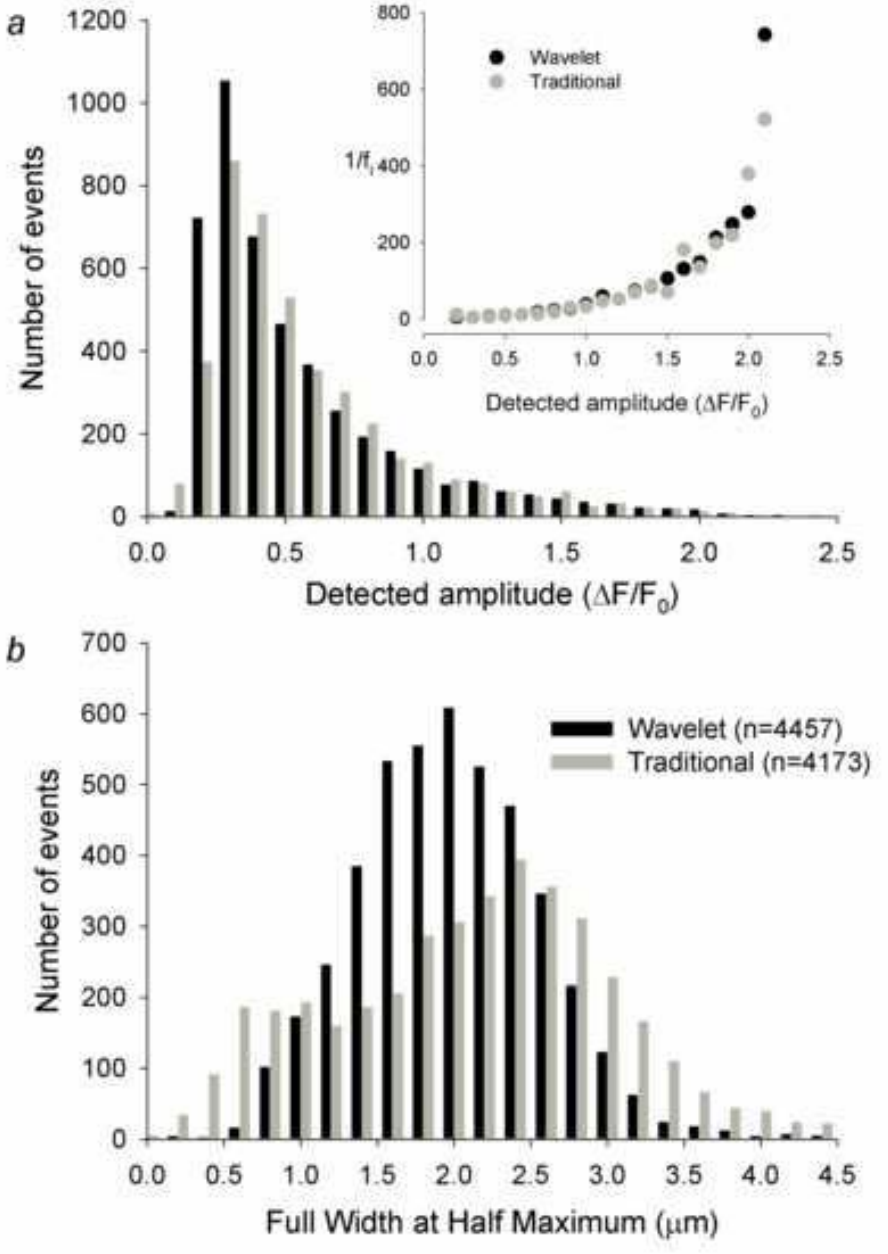

Figure 6

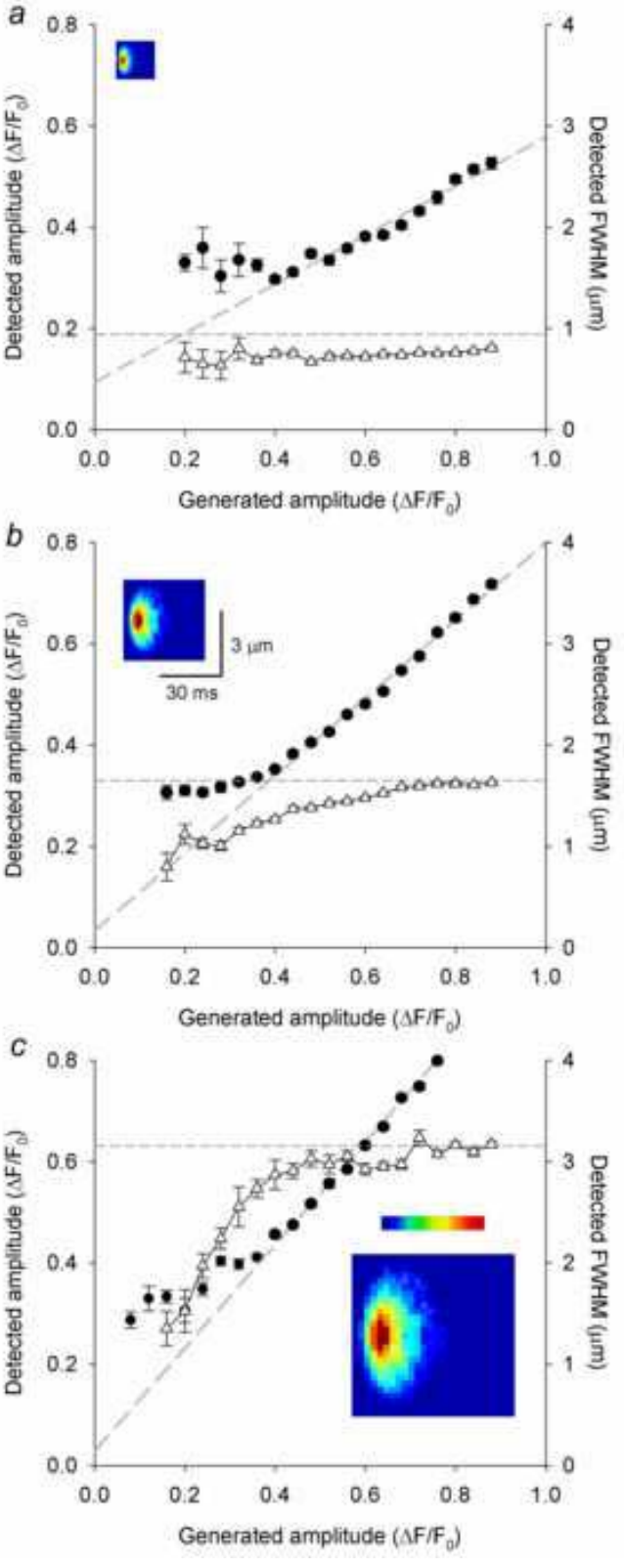

Figure 7

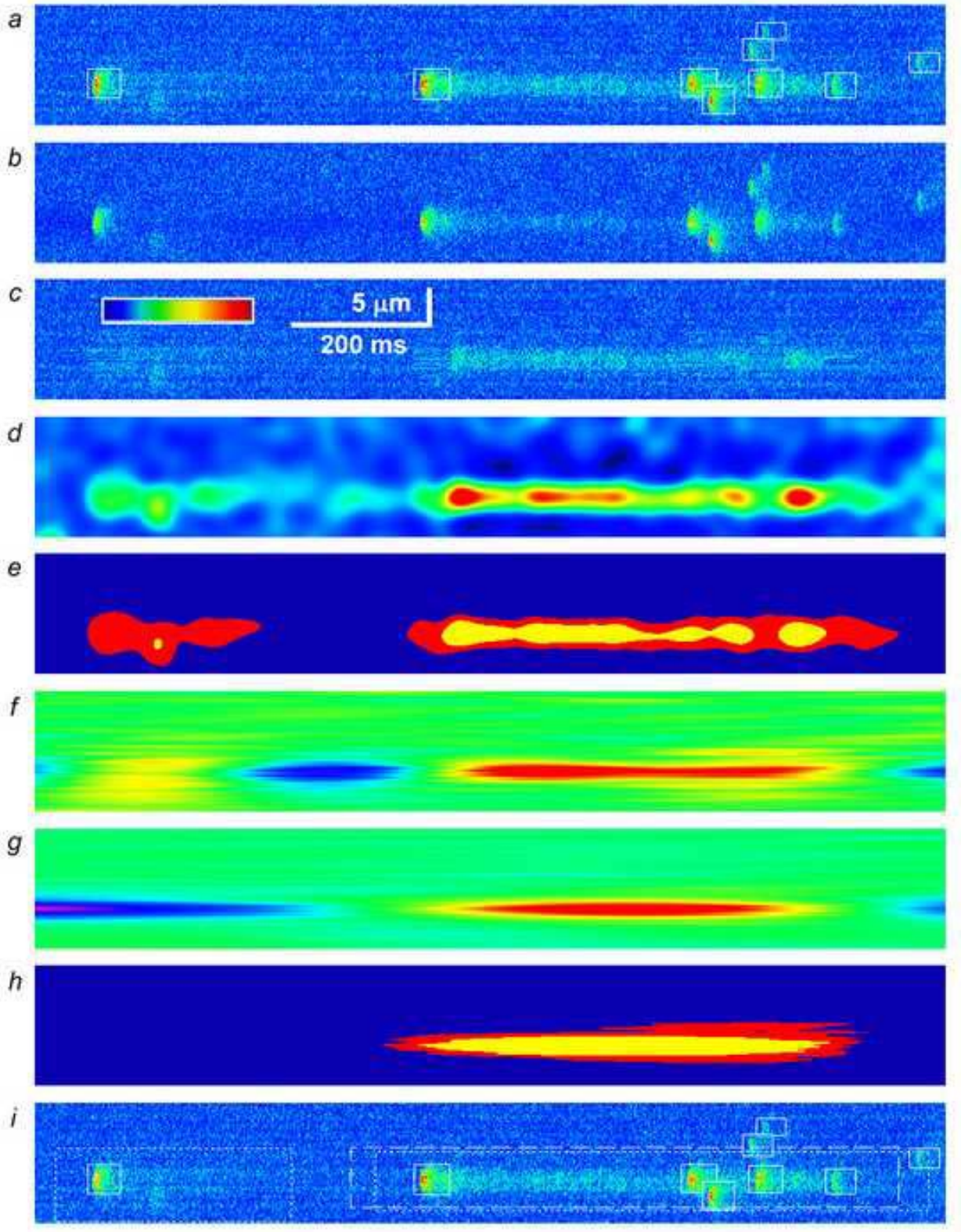

Figure 8

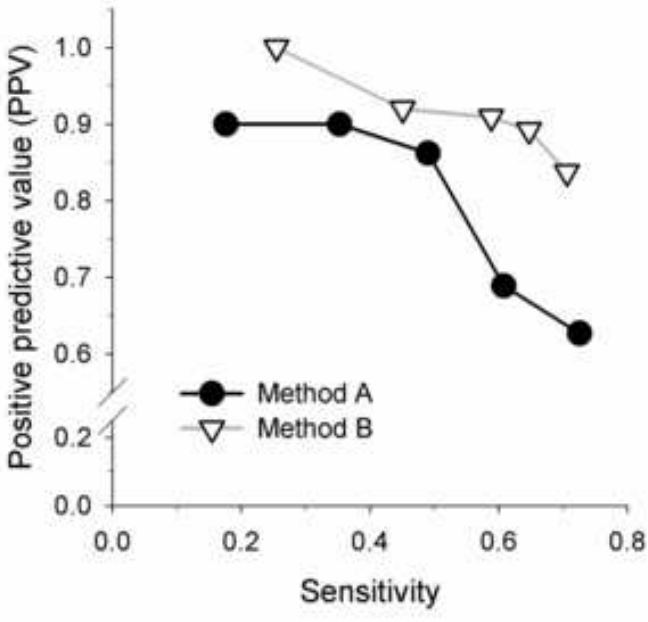

Figure 9